Materials & Design 240 (2024) 112865

Contents lists available at ScienceDirect

Materials & Design

journal homepage: www.elsevier.com/locate/matdes

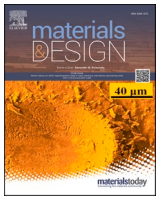

Mechanical softening of CuX alloys at elevated temperatures studied via high temperature scanning indentation

Marcel Sos [a,*], Gabrielle Tiphene [b,c], Jean-Luc Loubet [b], Sebastian Bruns [a], Enrico Bruder [a], Karsten Durst [a]

[a] Technical University Darmstadt, Physical Metallurgy, Peter-Grünberg-Straße 2, 64287 Darmstadt, Germany
[b] Univ Lyon, Ecole Centrale de Lyon, CNRS, ENTPE, LTDS, UMR5513, 69130 Ecully, France
[c] Mines Saint-Etienne, CNRS, UMR 5307 LGF, Centre SMS, F – 42023 Saint-Etienne, France

ARTICLE INFO

Keywords:
Nanoindentation
High Temperature
Mechanical Properties
Ultrafine-grained microstructure
Strain rate sensitivity

ABSTRACT

The thermal stability and temperature dependent hardness of ultrafine-grained Cu-alloys CuSn5 and CuZn5 after high pressure torsion are investigated using the high temperature scanning indentation (HTSI) method. Fast indentations are carried out during thermal cycling of the samples (heating-holding-cooling) to measure hardness and strain rate sensitivity as a function of temperature and time. The microstructures after each thermal cycle are investigated to characterize the coarsening behaviour of both alloys.

Results show that the thermal stability of the tested alloys can be expressed in terms of several temperature regimes: A fully stable regime, a transient regime in which growth of individual grains occurs, and finally a regime in which the microstructure is fully coarsened. The onset of grain growth is accompanied by high strain rate sensitivity on the order of 0.2–0.3. Furthermore, the obtained hardness and strain rate sensitivity values are in good agreement with continuous stiffness measurement (CSM) and strain rate jump (SRJ) experiments. This highlights the applicability of the HTSI method to the characterization of the thermomechanical properties of ultrafine-grained alloys.

1. Introduction

Ultrafine-grained (UFG) materials with a grain size below 1 μm, obtained in bulk by utilizing severe plastic deformation methods like equal channel angular pressing (ECAP) or high pressure torsion (HPT) [1–3], offer interesting properties compared to their coarse-grained counterparts, such as increased strength, pronounced strain rate sensitivity and potential superplasticity [4–11]. This can be attributed to the increased density of grain boundaries [12–15]. At elevated temperatures, the strain rate sensitivity further increases and significant softening can be observed. UFG materials may even become softer than coarse-grained ones [8,16–20].

Additionally, the large strains imposed during processing induce a high density of defects [21–23]. As a result, high driving forces for relaxation and coarsening processes exist, which can limit the thermal stability of UFG microstructures to the point where property changes may already occur at room temperature [5,24–28].

This necessitates the investigation of thermal stability limits of such materials. In literature this is usually done via hardness measurements at room temperature after annealing [29–31]. This provides information on the temperature ranges in which changes occur, but not on the mechanical properties at elevated temperatures. To this end, high temperature nanoindentation can be utilized. Classical high temperature nanoindentation requires a lengthy tip and sample temperature matching procedure at each testing temperature [32,33], during which changes in the sample material may already take place. Additionally, both methods mentioned above only provide a limited time and temperature resolution, as high temperature indentation studies are typically performed with temperature steps in the range of 50–100 °C [32,34–36].

In this work, the high temperature scanning indentation (HTSI) method introduced by Tiphene et al. [37–39] is used to investigate the thermal stability of UFG copper alloys CuSn5 and CuZn5 processed via HPT. They were selected to follow up previous studies on CuX alloy systems.

In a publication by Bruder et al. [40], the saturation grain size after

* Corresponding author.
E-mail address: marcel.sos@tu-darmstadt.de (M. Sos).

https://doi.org/10.1016/j.matdes.2024.112865
Received 22 December 2023; Received in revised form 20 February 2024; Accepted 18 March 2024
Available online 20 March 2024

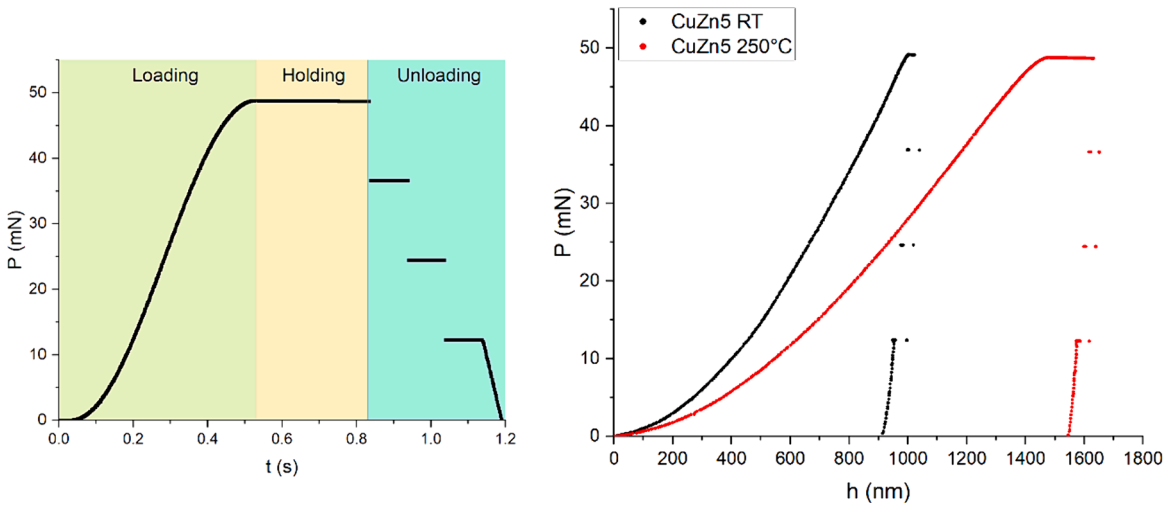

Fig. 1. A representative load-time-curve (left) and two load–displacement-curves recorded on CuZn5 at room temperature and 250 °C (right).

HPT, as well as the room temperature hardness and strain rate sensitivity were investigated. CuSn5 showed a grain size of 62 ± 26 nm, while the grain size of CuZn5 was found to be 304 ± 142 nm.

A publication by Keil et al. [29] then presented room temperature hardness measurements after isochronal annealing of HPT samples at different temperatures. Despite its much smaller grain size, CuSn5 showed a higher thermal stability than CuZn5.

The HTSI method utilizes rapid indentations on the order of 1 s per test, which are performed during heating, holding at elevated temperature and cooling to characterize hardness and strain rate sensitivity as a function of temperature and time. Tests are performed with different target temperatures and holding times to probe the thermal stability limits of the alloys.

2. Experimental methodology

2.1. Sample preparation

HPT samples with a diameter of 20 mm and an initial height of 4 mm were prepared from CuSn5 and CuZn5 rods provided by Wieland-Werke AG (Germany). The used HPT anvils had a cavity diameter of 20 mm and height of 1.5 mm each. A pressure of 4.6 GPa was applied and 30 rotations were done with a speed of 1 rpm using a HPT press by W. Klement GmbH (Austria). A cooling ring was mounted to the upper anvil to keep the process temperature close to ambient.

The deformed disks were cut into 4 equally sized parts and the sample surfaces were mechanically ground and polished to 1 μm diamond suspension, followed by a fine polishing step using Buehler MasterMet 2 colloidal silica suspension (0.02 μm). One part of the disk was used for the temperature adjustment procedure while the remaining three were each used to test one of the three thermal profiles described in the following section.

2.2. Experimental procedure

Nanoindentation testing was performed using a KLA InSEM-HT nanoindenter, capable of continuous stiffness measurement (CSM). CSM was used during reference measurements shown in the appendix, but not during the HTSI tests. A diamond Berkovich tip (Synton-MDP) was used, which has previously been calibrated on fused silica according to the Oliver-Pharr method [41]. The indenter system is mounted inside a TESCAN VEGA3 SEM and testing was carried out under vacuum (10^{-2} Pa).

The HTSI tests were performed during thermal ramping (heating-holding-cooling) following the procedure described by Tiphene et al. in [37,39]. The indentation loading curve follows a half-sinus profile described by

$$P(t) = \frac{P_{max}}{2}\left(1 + \sin\left(\frac{\pi}{t_{load}}t - \frac{\pi}{2}\right)\right) \quad (1)$$

with the target load P_{max} and the loading time t_{load}. In this study, a loading time of $t_{load} = 0.5$ s was chosen. The maximum load was held for 0.3 s, followed by a stepwise unloading. The loading protocol is described in greater detail in [39].

Fig. 1 (left) shows an example of the load-time-curve with P_{max} = 50 mN. On the right, two representative load–displacement-curves for CuZn5 recorded at room temperature and 250 °C can be seen.

A linear fit of the unloading branch of the force–displacement-curve is used to obtain the raw unloading stiffness

$$S = \frac{dF}{du} \quad (2)$$

This value is then corrected for the load frame stiffness S_{frame} via

$$S_u = \frac{1}{\frac{1}{S} - \frac{1}{S_{frame}}} \quad (3)$$

assuming a constant frame stiffness for all tests [33]. The contact depth h_c is then obtained from [42].

$$h_c = h_{max} - 0.75\frac{P_{max}}{S_u} \quad (4)$$

using the maximum depth and load h_{max} and P_{max}.

The contact area A_c for a Berkovich indenter is defined as

$$A_c = m_0 {h_c}^2 + m_1 h_c + m_2 {h_c}^{1/2} \cdots = \sum_{i=0}^{n} m_i {h_c}^{2^{1-i}} \quad (5)$$

with coefficients m_i obtained from calibrating the tip area function on fused silica.

The contact area at maximum depth is used to calculate the hardness

$$H = \frac{P_{max}}{A_c} \quad (6)$$

and reduced modulus

$$E_R = \frac{S_u}{2}\sqrt{\frac{\pi}{A_c}} \quad (7)$$

The elastic modulus of the sample is then given by [43].

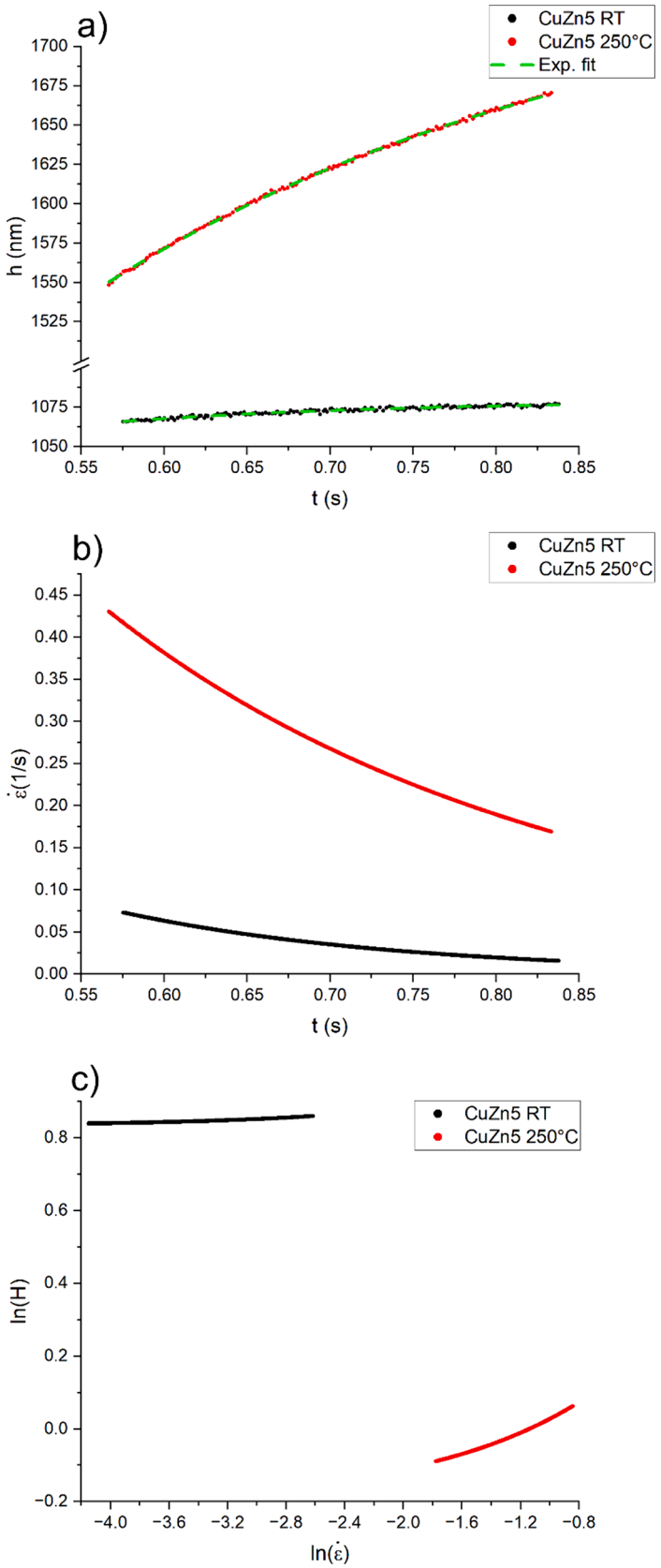

Fig. 2. Representative curves showing depth over time during the holding segment (a), the computed strain rates (b) and the ln(hardness)-ln(strain rate)-graph used for the calculation of m (c) for CuZn5 at room temperature and 250 °C.

Table 1
Test parameters for the HTSI ramps.

Material	Sample Heating Rate	P target	h target	T_{max}	t_{hold}
CuSn5	5.13 °C/min	50 mN	/	400 °C	2 h
		/	1000 nm	200 °C	6 h
		/	1000 nm	300 °C	0 h
CuZn5	5.21 °C/min	50 mN	/	400 °C	2 h
		/	1000 nm	200 °C	4 h
		/	1000 nm	300 °C	0 h

$$E = \frac{1-\nu^2}{\frac{1}{E_R} - \frac{1-\nu_{tip}^2}{E_{tip}}} \tag{8}$$

with the Poisson ratio of tip ν_{tip} and sample ν and the tip elastic modulus E_{tip}. The tip modulus is corrected for temperature according to Wheeler and Michler [44].

To obtain the coefficient of strain rate sensitivity m, the load–displacement-data recorded during the holding segment is used. The change in displacement over time $h(t)$ is fit using an exponential function of the form

$$h_{fit} = A_1 \exp\left(-\frac{t_{hold}}{t_1}\right) + h_0 \tag{9}$$

with the time t_{hold} and the function coefficients A_1, t_1 and h_0. The coefficients of the fit are used in the derivative function

$$\dot{h_{fit}} = -\frac{A_1}{t_1} \exp\left(-\frac{t_{hold}}{t_1}\right) \tag{10}$$

to calculate the indentation strain rate $\dot{\varepsilon} = \dot{h_{fit}}/h_{fit}$ (11). Hardness during the holding segment is calculated as

$$H = \frac{P}{A_{chold}} \tag{12}$$

using the load during holding P. The contact depth is given by

$$h_{chold} = h_{fit} - 0.75\frac{P}{S_u}$$

Finally, the strain rate sensitivity $m = \frac{d\ln(H)}{d\ln(\dot{\varepsilon})}$ (14) is calculated via a linear fit.

Fig. 2(a) shows representative h(t) data and the applied exponential fit, as well as the resulting strain rates (b) and the ln(H)-ln($\dot{\varepsilon}$)-curves used for the calculation of m (c).

One sacrificial sample of each material was used to calibrate the offset between T_{tip} and T_{sample} at the maximum testing temperature of T_{tip} = 400 °C according to the temperature matching procedure described by Minnert et al. [33]. The heating rates for tip and sample were chosen so that both reach their respective target temperature at the same time. The sample temperature was measured via a thermocouple placed in a molybdenum sheet between the sample heater and the bottom surface of the sample, while the tip thermocouple was mounted on the shaft in close proximity to the tip. The temperature of the probed sample surface was assumed to be equal to the tip temperature.

Table 1 lists the parameters for the thermal ramps used in this study. Tip and sample were simultaneously heated at the given rates until the maximum temperature was reached, followed by holding for the designated time and lastly cooling back to room temperature at the same rates. The tip was heated at a rate of 5 °C/min in every test. The holding period for the CuZn5 200 °C sample was shorter than for CuSn5 due to an unplanned early shutdown of the heating system.

For the samples heated to 400 °C, all indents were done to a set maximum load, resulting in varying depths throughout the duration of the test, ranging from 840 nm to 2100 nm. The hardness is expected to be independent of depth in this range. Representative data from CSM measurements is shown in the appendix. Measurements on the 200 °C and 300 °C series were carried out with an updated version of the method, in which the target load is adjusted after each indent to reach an approximately constant depth. Indents were placed 40 μm apart to avoid an influence of overlapping plastic zones.

Additionally, reference continuous stiffness measurement (CSM) and strain rate jump (SRJ) indentation tests were performed at room temperature before and after each thermal cycle. The details can be found in the appendix.

Microstructural analysis was carried out using a TESCAN MIRA3 SEM equipped with a Deben 4 quadrant BSE detector, operating at an acceleration voltage of 20 kV.

3. Results & discussion

3.1. 200 °C cycle: Reversible mechanical softening

In the following, filled symbols in plots over temperature denote the heating and holding segments, while open symbols indicate the cooling segment. Fig. 3 shows that the initial hardness at room temperature is approximately 4.5 GPa for CuSn5 and 2.6 GPa for CuZn5. As the temperature increases to 200 °C, H decreases to 3.75 GPa (-17 %) and 1.5 GPa (-43 %) respectively. For both samples the hardness remains constant throughout the holding period. After cooling to room temperature, the hardness returns to its initial value, which indicates a good thermal stability of the analysed alloys at the selected temperature. The microstructural observations (Fig. 9) will be discussed in detail in section 3.4. It is worth mentioning that the CuSn5 sample shows a significantly higher scatter in the measured hardness values.

In Fig. 4 it can be seen that both samples show rate sensitivities in the range of 0.01–0.02 at room temperature, which increases up to m = 0.1 (CuZn5) and 0.06 (CuSn5) at 200 °C. A slight decrease of m during the holding period is observed for both samples, which could be a measurement artifact resulting from thermal nonequilibrium.

Upon cooling, the coefficient of strain rate sensitivity m decreases and returns back to its initial value for both alloys. The hardness and strain rate sensitivity values at room temperature are in good agreement with previous results by Bruder et al. and Keil et al. [29,40]. Ultrafine-grained fcc metals are known to exhibit pronounced strain rate sensitivity, which increases with decreasing grain size and increasing temperature. This is generally attributed to the high density of grain boundaries [6,8,12–15,17,18,45]. The initial increase in strain rate sensitivity upon cooling of the CuZn5 sample, as well as the pronounced split between the heating and cooling branches seen in Fig. 4(b), can be attributed to the uncontrolled cooling of the sample after the shutdown of the heater.

3.2. 300 °C cycle: Kinking heating & cooling branches

This HTSI cycle was performed without a holding period at maximum temperature in order to observe transient behaviour without giving the microstructure enough time to coarsen.

During heating to 300 °C, CuZn5 exhibits a linear hardness decrease, but during cooling a change in the slope can be seen at a temperature of approximately 175 °C (Fig. 5). The room temperature hardness after the heating cycle is decreased by 19 % compared to the initial state. The CuSn5 sample, in contrast, shows a change in slope at 200 °C, which is followed both during heating and cooling. It also exhibits a slight residual hardness decrease of 4.5 %.

Fig. 6 shows that the coefficient of strain rate sensitivity m increases with temperature from a value of 0.02 at room temperature and reaches maximum values of 0.2 for CuZn5 at a temperature of 275 °C and 0.3 for CuSn5 at 300 °C. This increase of one order of magnitude indicates a significant effect of temperature on the mechanical behaviour. The cooling branch is offset to slightly lower values for CuZn5 and to higher values for CuSn5. This difference could be caused by different effective

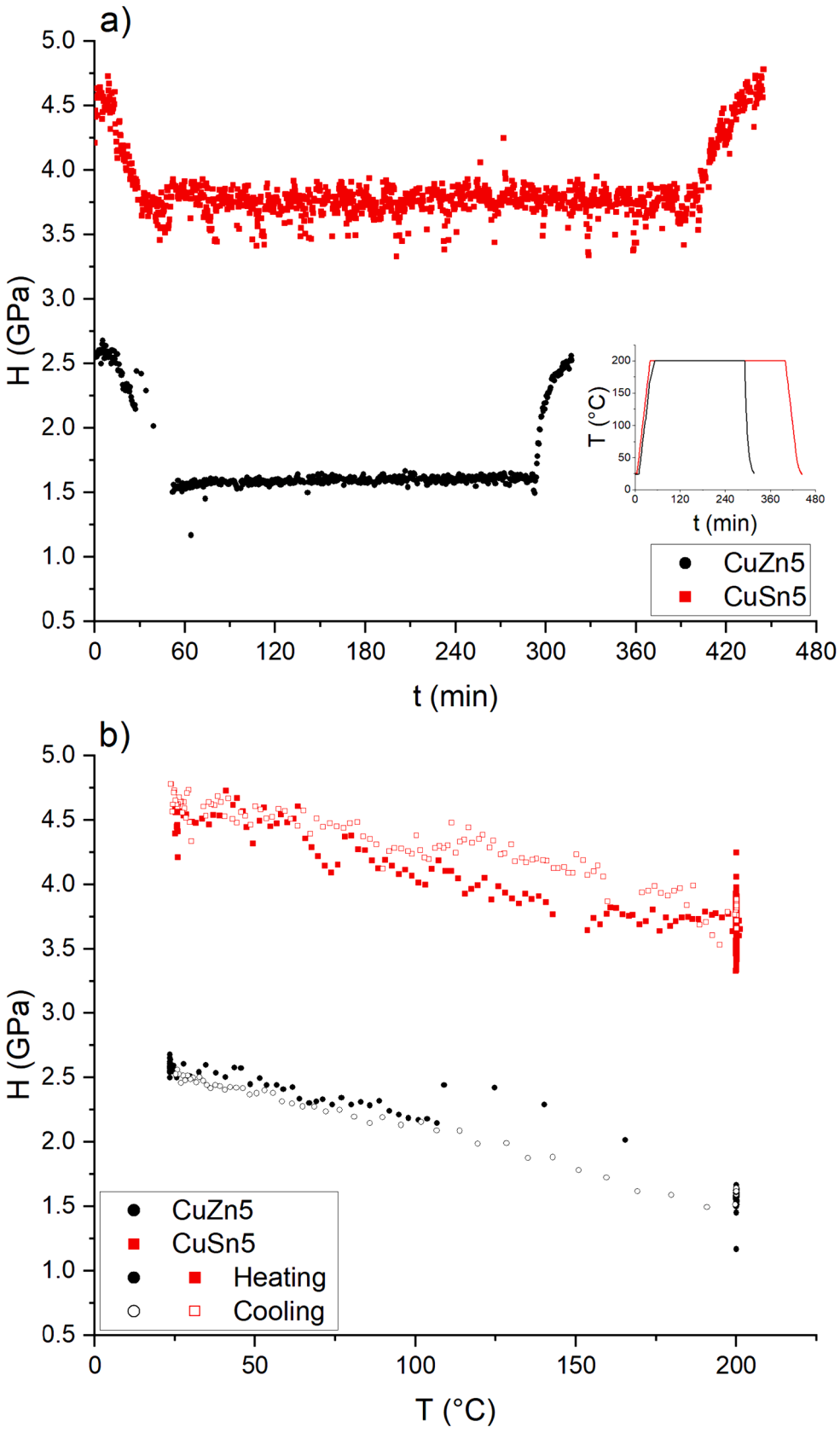

Fig. 3. Hardness as a function of time (a) and temperature (b) for the 200 °C thermal cycle. The inset in (a) shows the temperature ramp over time.

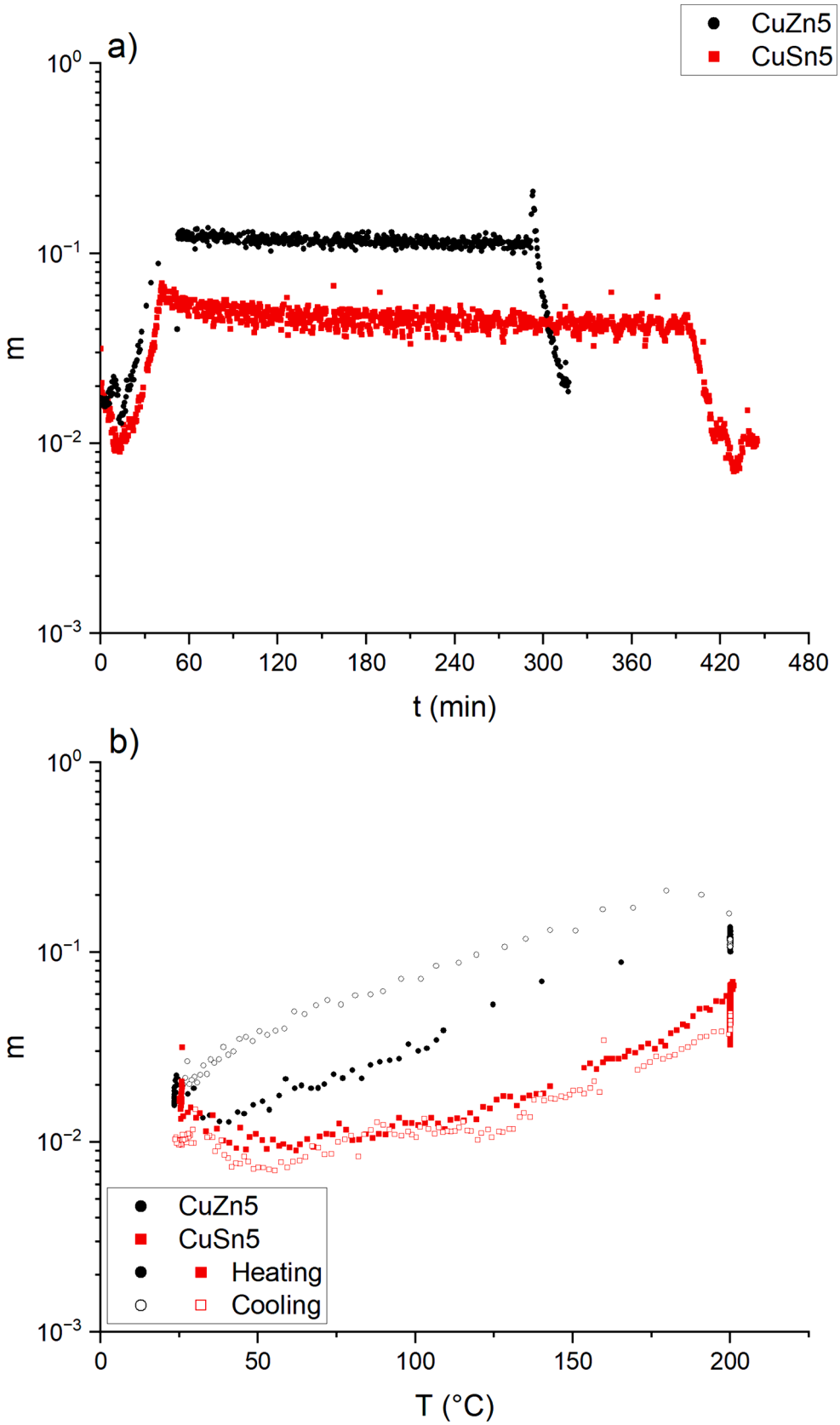

Fig. 4. Strain rate sensitivity as a function of time (a) and temperature (b) during the 200 °C thermal cycle.

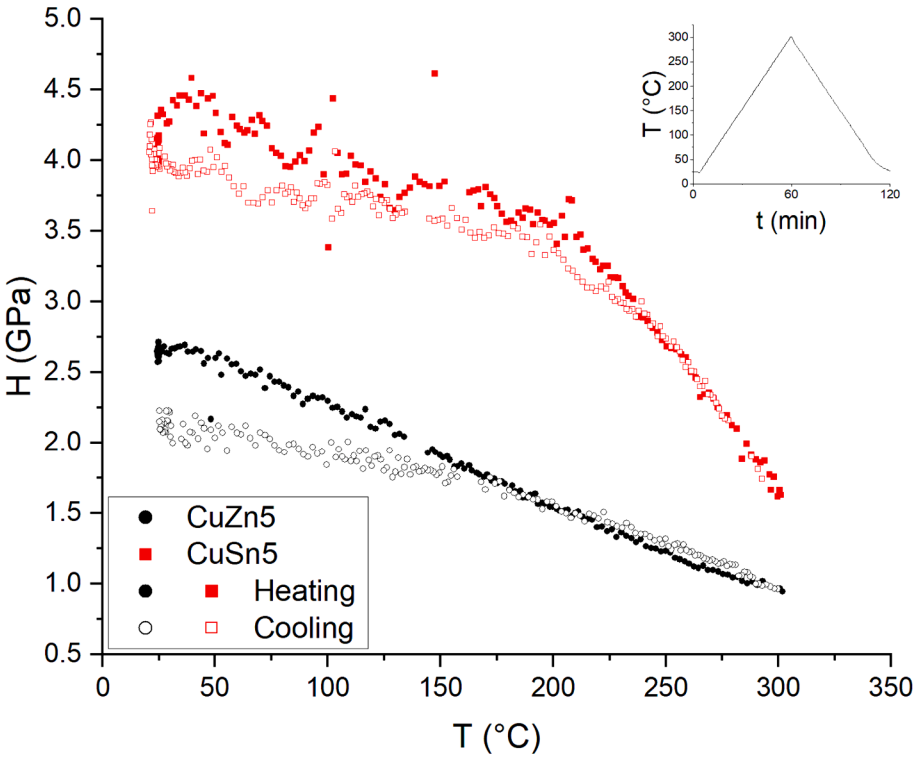

Fig. 5. Hardness as a function of temperature during the 300 °C cycle.

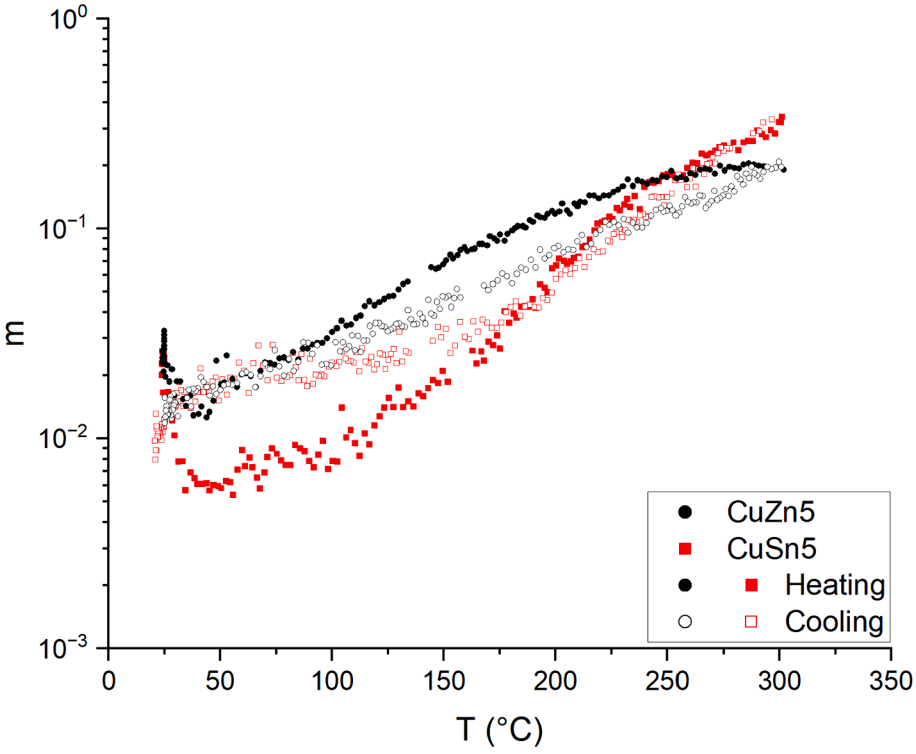

Fig. 6. Strain rate sensitivity as a function of temperature during the 300 °C cycle.

heating and cooling rates of the tip and sample.

3.3. 400 °C cycle: Significant mechanical softening

This thermal profile was selected to map the mechanical properties of both alloys up to a temperature at which a significant decrease in room temperature hardness is expected. For CuZn5 a linear decrease in hardness can be observed until a temperature of approximately 275 °C, at which the curve kinks and the slope is reduced (Fig. 7). The hardness remains constant during the holding period and the cooling slope is

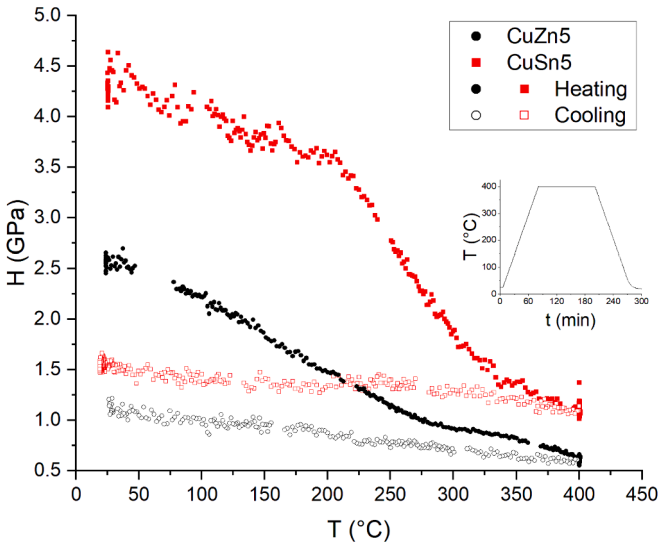

Fig. 7. Hardness as a function of temperature during the 400 °C cycle.

linear. CuSn5 on the other hand shows two changes in slope during heating. The first change occurs at a temperature of approximately 200 °C, resulting in increased softening as the temperature is further increased. The second change can be seen at a temperature of approximately 325 °C. Similar to CuZn5, the H(T) curve becomes less steep at this point. The hardness is constant during holding and increases linearly during cooling. CuSn5 shows higher scatter until the first slope change, at which it decreases significantly.

Fig. 8 shows an increase of the strain rate sensitivity with increasing temperature, from its initial values of approximately 0.02 up to a maximum of 0.2 at 275 °C (CuZn5) and 0.3 at 325 °C (CuSn5), corresponding to the temperatures at which changes in the H(T) slope are observed (Fig. 7). An increase in temperature past this maximum results in a decreasing m, which then further decreases during holding at 400 °C.

During cooling the strain rate sensitivity of CuZn5 decreases linearly in the semilogarithmic plot, while significant scatter is observed for CuSn5. For both samples the m values recorded during cooling are lower than during heating. At room temperature m then reaches values of approximately 0.01 for both alloys.

Hardness and strain rate sensitivity are not shown as a function of time for this cycle, as the hardness remains constant during the holding segment at 400 °C while the coefficient of strain rate sensitivity decreases. As noted in section 3.1, this could be a measurement artifact caused by slow thermal equilibration.

3.4. Microstructural evolution during the HTSI cycles

The initial microstructural conditions (Fig. 9 a,b) of the investigated alloys were determined in a previous publication, where the HPT saturation grain sizes were found to be 62 ± 26 nm (CuSn5) and 304 ± 142 nm (CuZn5) via transmission Kikuchi diffraction (TKD) and electron backscatter diffraction (EBSD) respectively [40].

After the 200 °C thermal cycle (c,d) no observable microstructural changes have taken place compared to the reference state. After the 300 °C cycle coarsening can be observed in both microstructures (e,f). In the case of CuSn5 the growth of individual grains to a size of approximately 250 nm can be seen. For CuZn5, some grains with a diameter on the order of 1–2 μm are found, surrounded by an ultrafine-grained matrix. The grain size distribution appears to become bimodal.

Both microstructures are significantly coarsened after the 400 °C cycle (g,h). Thermal etching artifacts are visible for both alloys, but more pronounced for CuSn5. This makes an exact visual determination of the grain size difficult, but it can be approximated to be in the range of 4–10 μm for CuZn5 and 1–5 μm for CuSn5. The etching artifacts were not polished off to preserve the indents for future pileup measurements.

Based on the measurements of hardness and strain rate sensitivity, as well as the microstructural observations, a schematical model of the thermal stability and coarsening behaviour of CuSn5 is presented in Fig. 10. It is split into three distinct stages, which can be attributed to

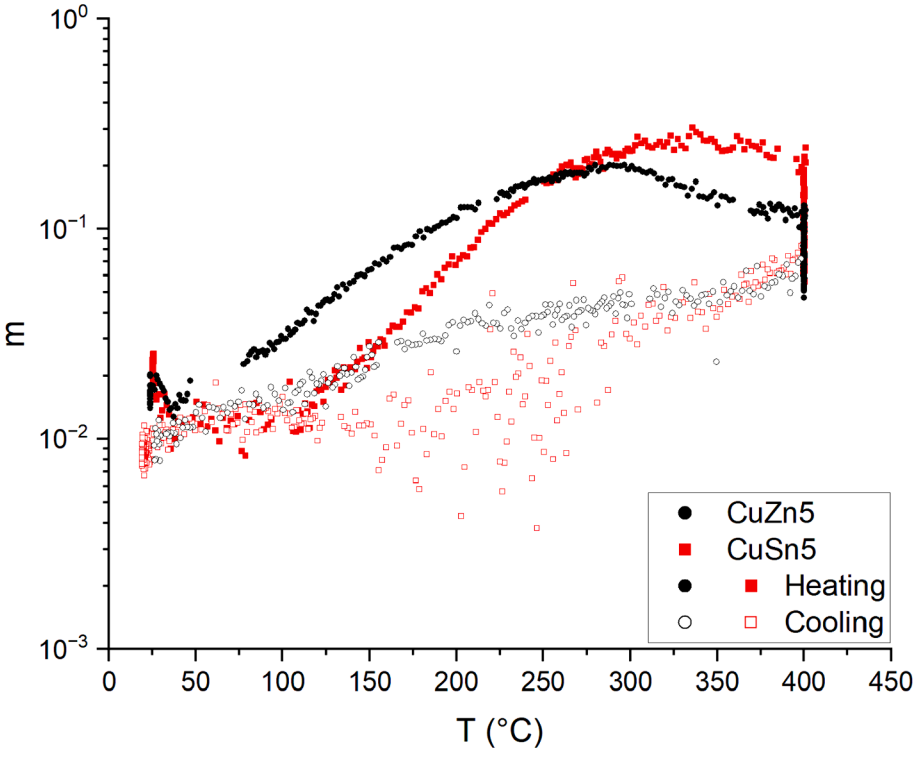

Fig. 8. Strain rate sensitivity as a function of temperature during the 400 °C cycle.

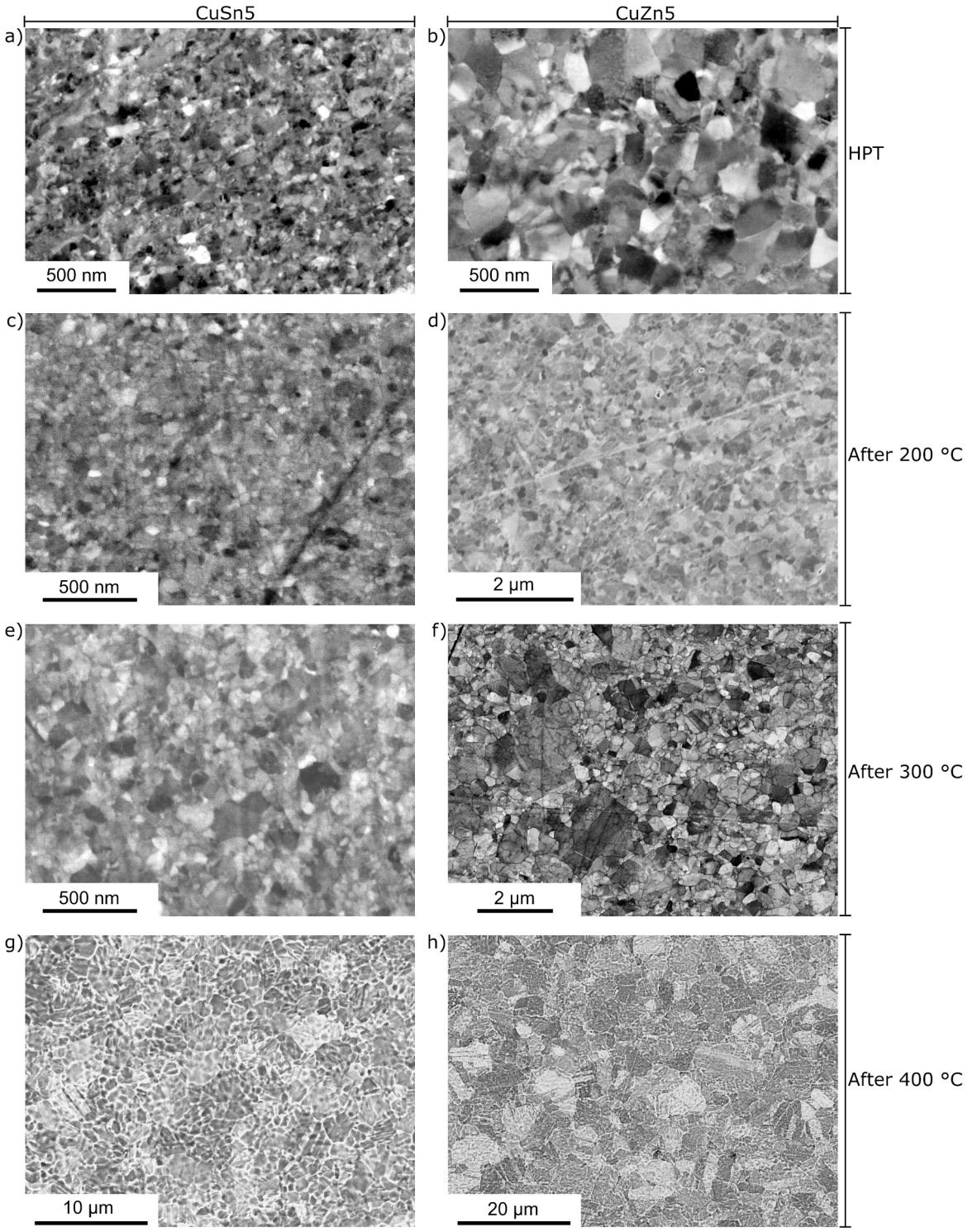

Fig. 9. BSE images of the sample microstructures of CuSn5 (left) and CuZn5 (right) in the initial (HPT) state, as well as after each thermal cycle.

different mechanisms.

In the first region, up to a temperature of 200 °C, both alloys are stable in the timeframes investigated in this study, as seen in Fig. 4, and the grain structure remains unchanged. The reversible decrease in hardness ΔH_{rev} can be explained by thermal softening due to the increased rate sensitivity [8,16–19], resulting from grain boundary mediated deformation and recovery processes in the plastic zone and a decrease of the dislocation density. The fact that the room temperature hardness remains unchanged indicates that these are thermomechanical processes requiring both elevated temperature as well as the deformation imposed by the indenter. This is supported by the sample microstructures remaining unchanged in regime I. Similarly, in a study on UFG-Au by Maier et al. [45] strain rate sensitivities of up to 0.3 were measured, along with pronounced reversible softening at elevated temperatures and no microstructural changes.

The second regime is characterized by a transient behaviour, seen in the hardness data recorded in the 300 °C cycle (Fig. 5), as well as the resulting microstructures (Fig. 9 e,f). In this temperature range, some

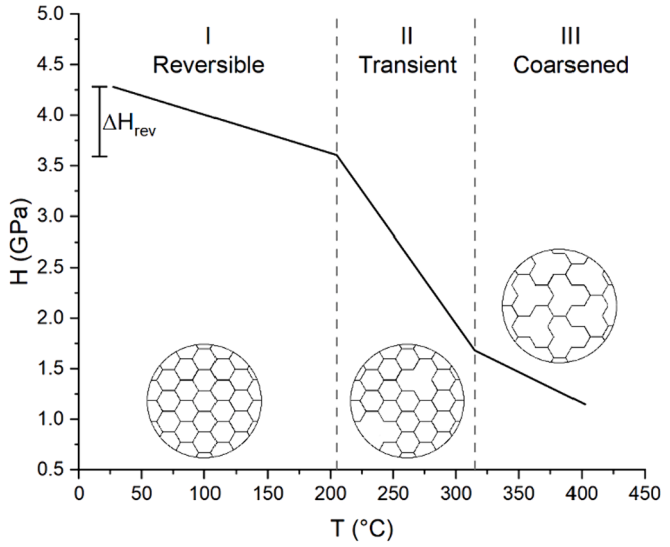

Fig. 10. Schematic representation of the three stages observed in the H(T) curve of CuSn5 during heating to 400 °C. Schematic microstructures not to scale.

grain growth can be seen while the surrounding microstructure is still stable with grain sizes comparable to the initial HPT state. Due to the partial coarsening, the room temperature hardness is reduced after the 300 °C thermal cycle. In the third regime, observed during heating to 400 °C (Fig. 7), significant grain growth takes place in both alloys. The irreversible hardness decrease in regimes 2 and 3 can be attributed to the thermal instability of the UFG microstructures.

The maximum in the coefficient of strain rate sensitivity (Fig. 8) corresponds to the transition from regime 2 to 3, indicating the highest microstructural instability and the onset of significant grain growth. As the grain size increases, m continuously decreases throughout regime 3, as the alloys lose their ultrafine-grained microstructure.

In literature, similar 3-segment curves have been shown for the room temperature hardness of UFG Al-alloys after quenching from DSC [30,31].

It remains unclear, however, why the transition from regime 1 to 2 can be seen in the H(T) curve of CuSn5 but not that of CuZn5. It could be related to different behaviour of the alloying elements and requires more in-depth investigations of the microstructural conditions, including TEM studies. The different initial grain size could also play a role.

The HTSI investigations further reveal that CuSn5 exhibits a higher thermal stability than CuZn5, despite its smaller initial grain size by a factor of 5, which should provide a larger driving force for coarsening processes. In CuSn5 grain growth sets in at a higher temperature (325 °C compared to 275 °C for CuZn5) and the residual hardness change after the 300 °C cycle is lower, only showing a 4.5 % reduction in hardness compared to the 19 % reduction seen for CuZn5. This is in line with a previous study, in which the hardness of CuX alloys was investigated after isochronal annealing at different temperatures [29]. In that work by Keil et al., the hardness of CuSn5 remained approximately constant after isochronal annealing for 1 h at temperatures up to 250 °C, while a slight decrease of 0.4 GPa was seen in CuZn5.

After the 400 °C cycle CuSn5 shows a 37 % higher residual hardness than CuZn5. This can be attributed to the significantly higher solid solution strengthening contribution of Sn compared to Zn [46], as well as the lower grain size after HTSI.

The increased hardness scatter of CuSn5 at temperatures below 200 °C could potentially be explained by local inhomogeneities or precipitates which dissolve with increasing solubility of Sn, as CuSn5 is supersaturated at room temperature [47].

4. Conclusion & outlook

In this study, the high temperature scanning indentation (HTSI) method was used to investigate the thermal stability of ultrafine-grained CuSn5 and CuZn5 alloys processed via high pressure torsion. The measured hardness and strain rate sensitivity values are in good agreement with those obtained from conventional CSM and SRJ tests. The results show:

1. HTSI can be utilized to probe the thermal stability of ultrafine-grained materials with high temperature and time resolution via measurements of hardness and strain rate sensitivity.
2. The observed microstructural changes of both tested alloys can be classified in terms of three distinct temperature ranges.
3. The initial stable regime is followed by a transient, in which individual grains grow, and lastly by coarsening of the entire microstructure.
4. The onset of grain growth is accompanied by a maximum in strain rate sensitivity on the order of 0.2–0.3.

Overall, the potential of HTSI for thermomechanical characterization has been demonstrated. The fast testing protocol enables high throughput experiments with different thermal profiles. Results obtained from HTSI with its high data density can be used to more accurately select conditions to investigate with other methods, such as TEM and DSC. This is particularly relevant for alloy design studies, in which the mechanical properties over a wide range of temperatures and times might be of interest.

Future work will focus in more detail on the differences between the CuX alloys, including TEM studies and an investigation of pileup behaviour.

CRediT authorship contribution statement

Marcel Sos: Writing – review & editing, Writing – original draft, Visualization, Validation, Methodology, Investigation. **Gabrielle Tiphene:** Writing – review & editing, Validation, Methodology, Investigation. **Jean-Luc Loubet:** Writing – review & editing, Supervision, Resources, Project administration, Conceptualization. **Sebastian Bruns:** Writing – review & editing, Methodology, Conceptualization. **Enrico Bruder:** Writing – review & editing, Conceptualization. **Karsten Durst:** Writing – review & editing, Supervision, Resources, Project administration, Methodology, Funding acquisition, Conceptualization.

Declaration of competing interest

The authors declare that they have no known competing financial interests or personal relationships that could have appeared to influence the work reported in this paper.

Data availability

Research data associated with this article is available on the TUdatalib repository under the DOI 10.48328/tudatalib-1371.

Acknowledgements

We acknowledge support by the Deutsche Forschungsgemeinschaft (DFG – German Research Foundation) under grant no. DU 424/11-2, and the Open Access Publishing Fund of Technical University of Darmstadt. The authors also thank Dr. Achim Kuhn (Wieland-Werke AG, Germany) for providing the CuX alloys.

Appendix

Reference measurements on fused silica

Figure 11 shows 12 load–displacement-curves recorded on fused silica at room temperature, using the HTSI method. The measurements were performed with the KLA HT1K indenter described in [33]. The target depth was set to 1500 nm and the maximum load was held for 0.7 s. It can be seen that the discrepancy between the tests is low, highlighting the reproducibility of the method. The obtained hardness, modulus and strain rate sensitivity values (H = 9.4 ± 0.06 GPa, E = 72.3 ± 0.28 GPa and m = 0.005 ± 0.001) are in line with literature reference results on fused silica [32,48,49].

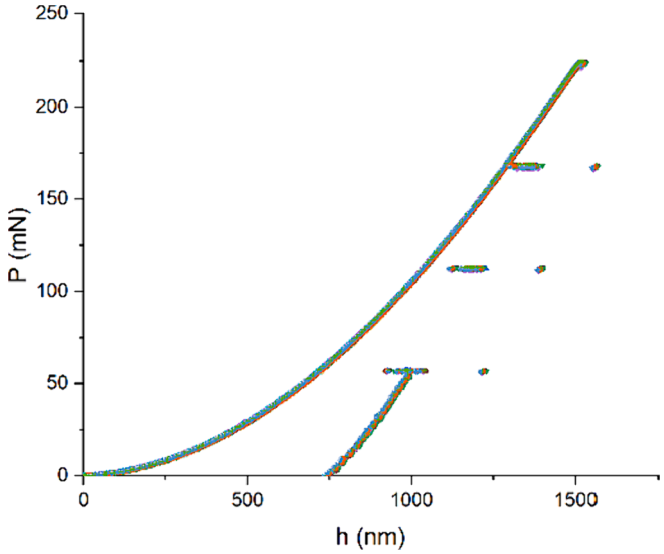

Fig. 11. Twelve overlaid load-displacement curves recorded on fused silica at room temperature using the HTSI method.

Validation of hardness and strain rate sensitivity results

Reference CSM measurements with an indentation strain rate of $\dot{\varepsilon} = \dot{h}/h = 0.2\,1/s$ were performed on each sample at room temperature using the same diamond tip used for the HTSI tests and a maximum load of 50 mN.

Strain rate jump (SRJ) tests according to Maier et al. [50] were performed at room temperature using a Keysight G200 nanoindenter equipped with a diamond Berkovich tip (Synton-MDP). The used strain rate sequence was $1x10^{-1}$ 1/s => $1x10^{-2}$ 1/s => $1x10^{-1}$ 1/s => $1x10^{-3}$ 1/s => $1x10^{-1}$ 1/s. The first strain rate jump was carried out at a depth of 500 nm, after which the segment length for each strain rate was 250 nm.

Table 2 shows a comparison of hardness and strain rate sensitivity values measured via CSM and SRJ tests at room temperature with the results from the HTSI cycles. For the HPT state, hardness values obtained from all samples before thermal cycling are averaged.

The hardness values measured via HTSI show the same trend as the CSM results: A significant decrease after the 400 °C cycle, a moderate decrease after the 300 °C cycle and no significant changes after the 200 °C cycle, correlating with the observed microstructural changes. The apparent decrease of the HTSI hardness after the 200 °C cycle is due to the aforementioned averaging.

The strain rate sensitivity is expected to follow a similar trend. It can be seen that, despite the significant difference in testing speed of 1 s per test for HTSI and 9 min per test for SRJ, the data is in decent agreement and, as mentioned in 3.1, in line with previous results. Differences can be explained by the rapid nature of the HTSI tests, while SRJ results can be affected by a non-constant hardness over depth and transients after the jumps, seen for example in [51].

Table 2
Room temperature hardness and strain rate sensitivity obtained from CSM and SRJ tests, as well as the HTSI method.

Material	Sample	H CSM (GPa)	H HTSI (GPa)	m SRJ	m HTSI
CuSn5	HPT	4.43 ± 0.11	4.34 ± 0.18	0.013 ± 0.001	0.020 ± 0.004
	After 200°	4.48 ± 0.06	4.63 ± 0.1	0.010 ± 0.001	0.010 ± 0.001
	After 300°	4.08 ± 0.05	3.98 ± 0.26	0.016 ± 0.0003	0.012 ± 0.002
	After 400°	1.69 ± 0.07	1.55 ± 0.05	0.016 ± 0.005	0.009 ± 0.001
CuZn5	HPT	2.66 ± 0.06	2.59 ± 0.05	0.027 ± 0.003	0.020 ± 0.004
	After 200°	2.68 ± 0.05	2.51 ± 0.03	0.019 ± 0.001	0.024 ± 0.004
	After 300°	2.21 ± 0.1	2.13 ± 0.06	0.022 ± 0.006	0.015 ± 0.002
	After 400°	1.18 ± 0.06	1.13 ± 0.05	0.012 ± 0.001	0.010 ± 0.001

Depth independence of hardness

In Figure 12 it can be seen that for both CuZn5 and CuSn5 the hardness remains approximately constant with increasing indentation depth. An indentation strain rate of 0.05 1/s was used.

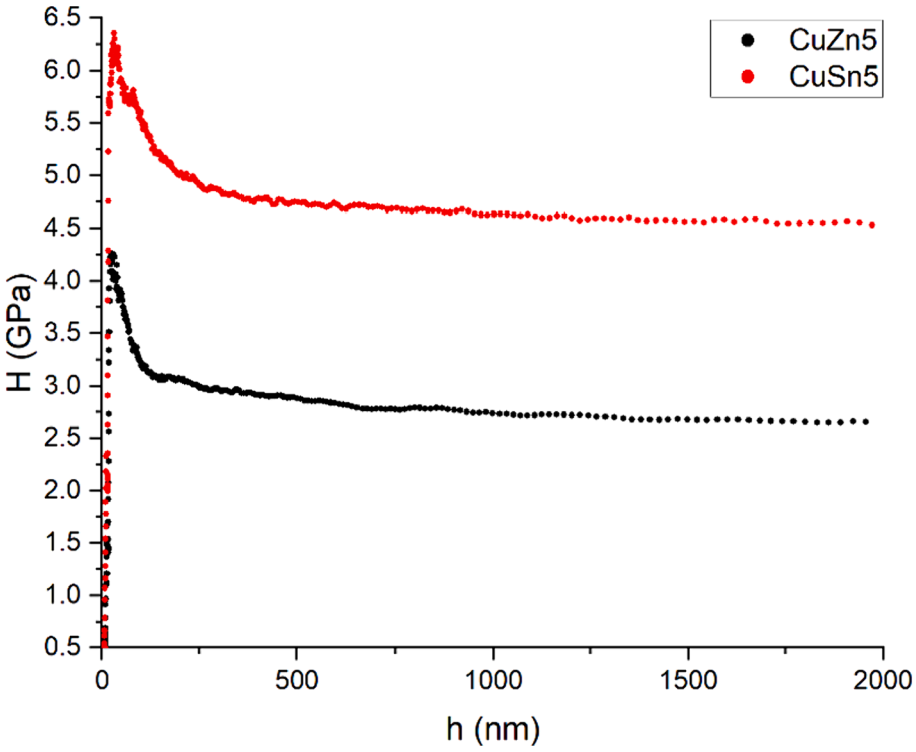

Fig. 12. Representative hardness-depth-curves for CuZn5 and CuSn5 in the HPT state at room temperature, recorded on the G200 nanoindenter described in the previous section.

Young's modulus data

Figure 13 shows the Young's modulus of fused silica and UFG CuSn5 measured by the HTSI method on the HT1K system. The used heating rate was 5 °C/min for the silica sample and 3 °C/min for the CuSn5 sample. It can be seen that there is a split between the heating and cooling branches and a larger scatter for the CuSn5 sample. This indicates that the determination of the unloading stiffness is sensitive to the heating cycle (and therefore the stability of the heater's PID control) and possibly the thermal conductivity of the sample material. The influence of this on the determination of the hardness is expected to be low.

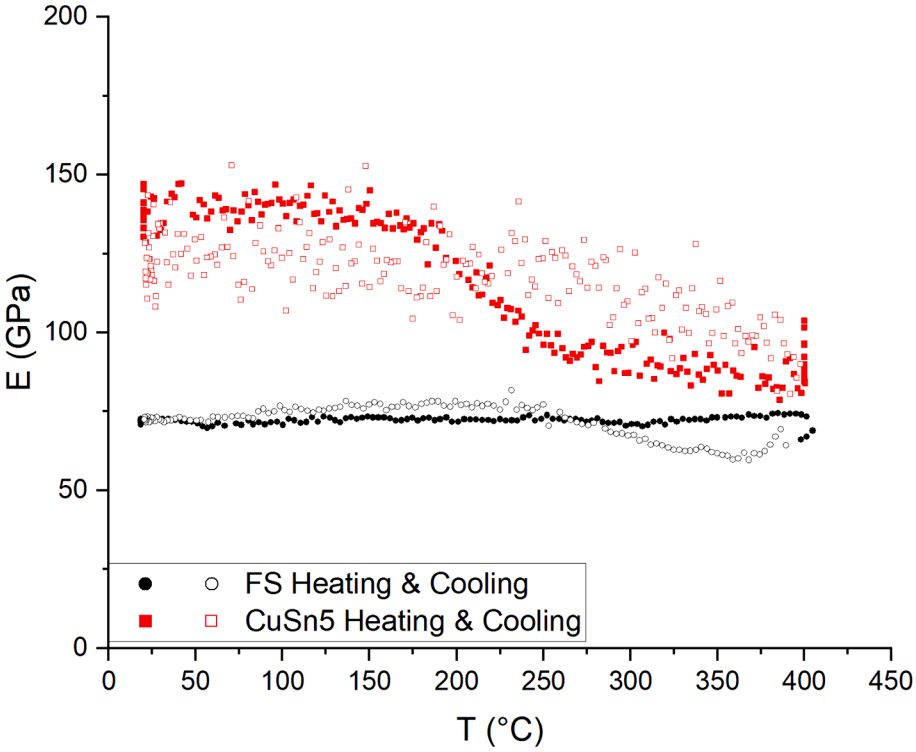

Fig. 13. Young's modulus of fused silica (FS) and UFG CuSn5 as a function of temperature.

References

[1] R. Valiev, et al., Bulk nanostructured materials from severe plastic deformation, Prog. Mater Sci. 45 (2) (2000) 103–189, https://doi.org/10.1016/S0079-6425(99)00007-9.

[2] K. Edalati, Z. Horita, A review on high-pressure torsion (HPT) from 1935 to 1988, Mater. Sci. Eng. A 652 (2016) 325–352, https://doi.org/10.1016/j.msea.2015.11.074.

[3] A.P. Zhilyaev, T.G. Langdon, Using high-pressure torsion for metal processing: fundamentals and applications, Prog. Mater Sci. 53 (6) (2008) 893–979, https://doi.org/10.1016/j.pmatsci.2008.03.002.

[4] R.Z. Valiev, et al., Paradox of strength and ductility in metals processed by severe plastic deformation, J. Mater. Res. 17 (1) (2002) 5–8, https://doi.org/10.1557/JMR.2002.0002.

[5] Y. Estrin, A. Vinogradov, Extreme grain refinement by severe plastic deformation: a wealth of challenging science, Acta Mater. 61 (3) (2013) 782–817, https://doi.org/10.1016/j.actamat.2012.10.038.

[6] Q. Wei, Strain rate effects in the ultrafine grain and nanocrystalline regimes—influence on some constitutive responses, J. Mater. Sci. 42 (5) (2007) 1709–1727, https://doi.org/10.1007/s10853-006-0700-9.

[7] T.G. Langdon, Twenty-five years of ultrafine-grained materials: achieving exceptional properties through grain refinement, Acta Mater. 61 (19) (2013) 7035–7059, https://doi.org/10.1016/j.actamat.2013.08.018.

[8] J. May, et al., Strain rate sensitivity of ultrafine-grained aluminium processed by severe plastic deformation, Scr. Mater. 53 (2) (2005) 189–194, https://doi.org/10.1016/j.scriptamat.2005.03.043.

[9] Y.M. Wang, E. Ma, Temperature and strain rate effects on the strength and ductility of nanostructured copper, Appl. Phys. Lett. 83 (15) (2003) 3165–3167, https://doi.org/10.1063/1.1618370.

[10] J. Kappacher, et al., Combination of nanoindentation and microscopy for the examination of aluminum alloys in Coarse- and ultrafine-grained condition, Prakt. Metallogr. 56 (7) (2019) 432–442, https://doi.org/10.3139/147.110571.

[11] R.B. Figueiredo, T.G. Langdon, Record superplastic ductility in a magnesium alloy processed by Equal-Channel Angular pressing, Adv. Eng. Mater. 10 (1–2) (2008) 37–40, https://doi.org/10.1002/adem.200700315.

[12] J. Bach, et al., Deformation mechanisms and strain rate sensitivity of bimodal and ultrafine-grained copper, Acta Mater. 186 (2020) 363–373, https://doi.org/10.1016/j.actamat.2019.12.044.

[13] J.M. Wheeler, et al., Activation parameters for deformation of ultrafine-grained aluminium as determined by indentation strain rate jumps at elevated temperature, Mater. Sci. Eng. A 585 (2013) 108–113, https://doi.org/10.1016/j.msea.2013.07.033.

[14] Q. Wei, et al., Effect of nanocrystalline and ultrafine grain sizes on the strain rate sensitivity and activation volume: fcc versus bcc metals, Mater. Sci. Eng. A 381 (1–2) (2004) 71–79, https://doi.org/10.1016/j.msea.2004.03.064.

[15] D. Torre, et al., Strain rate sensitivity and apparent activation volume measurements on equal channel angular extruded cu processed by one to twelve passes, Scr. Mater. 51 (5) (2004) 367–371, https://doi.org/10.1016/j.scriptamat.2004.05.021.

[16] Y.J. Li, et al., Transition from strengthening to softening by grain boundaries in ultrafine-grained cu, Acta Mater. 52 (17) (2004) 5009–5018, https://doi.org/10.1016/j.actamat.2004.07.003.

[17] A. Vevecka-Priftaj, et al., Strain rate sensitivity of ultrafine grained aluminium alloy AA6061, Mater. Sci. Forum 584–586 (2008) 741–747, https://doi.org/10.4028/www.scientific.net/MSF.584-586.741.

[18] A. Mishra, et al., High-strain-rate response of ultra-fine-grained copper, Acta Mater. 56 (12) (2008) 2770–2783, https://doi.org/10.1016/j.actamat.2008.02.023.

[19] W. Blum, Y.J. Li, Influence of grain boundaries on steady-state deformation resistance of ultrafine-grained cu, Phys. Stat. Sol. A 201 (13) (2004) 2915–2921, https://doi.org/10.1002/pssa.200406878.

[20] J. Bach, et al., Influence of grain boundaries on the deformation resistance: insights from an investigation of deformation kinetics and microstructure of copper after predeformation by ECAP, Philos. Mag. 93 (35) (2013) 4331–4354, https://doi.org/10.1080/14786435.2013.828161.

[21] Y.L. Wang, et al., Thermal behavior of copper processed by ECAP with and without back pressure, Mater. Sci. Eng. A 628 (2015) 21–29, https://doi.org/10.1016/j.msea.2015.01.021.

[22] H. Jiang, et al., Microstructural evolution, microhardness and thermal stability of HPT-processed cu, Mater. Sci. Eng. A 290 (1–2) (2000) 128–138, https://doi.org/10.1016/S0921-5093(00)00919-9.

[23] Y.B. Wang, et al., Dislocation density evolution during high pressure torsion of a nanocrystalline Ni–Fe alloy, Appl. Phys. Lett. 94 (9) (2009), https://doi.org/10.1063/1.3095852.

[24] E. Schafler, M.B. Kerber, Microstructural investigation of the annealing behaviour of high-pressure torsion (HPT) deformed copper, Mater. Sci. Eng. A 462 (1–2) (2007) 139–143, https://doi.org/10.1016/j.msea.2005.11.085.

[25] V.Y. Gertsman, R. Birringer, On the room-temperature grain growth in nanocrystalline copper, Scr. Metall. Mater. 30 (5) (1994) 577–581, https://doi.org/10.1016/0956-716X(94)90432-4.

[26] J. Čížek, et al., Thermal stability of ultrafine grained copper, Phys. Rev. B 65 (9) (2002), https://doi.org/10.1103/PhysRevB.65.094106.

[27] I. Roy, et al., Thermal stability in bulk cryomilled ultrafine-grained 5083 al alloy, Metall and Mat Trans A 37 (3) (2006) 721–730, https://doi.org/10.1007/s11661-006-0044-8.

[28] K. Edalati, et al., Long-time stability of metals after severe plastic deformation: softening and hardening by self-annealing versus thermal stability, Mater. Sci. Eng. A 729 (2018) 340–348, https://doi.org/10.1016/j.msea.2018.05.079.

[29] T. Keil, et al., Solid solution hardening effects on structure evolution and mechanical properties of nanostructured binary and high entropy alloys after high pressure torsion, IOP Conf. Ser.: Mater. Sci. Eng. 1249 (1) (2022) 12003, https://doi.org/10.1088/1757-899X/1249/1/012003.

[30] Y.H. Zhao, et al., Microstructures and mechanical properties of ultrafine grained 7075 al alloy processed by ECAP and their evolutions during annealing, Acta Mater. 52 (15) (2004) 4589–4599, https://doi.org/10.1016/j.actamat.2004.06.017.

[31] Y. Chen, et al., Microstructural evolution, strengthening and thermal stability of an ultrafine-grained Al–Cu–Mg alloy, Acta Mater. 109 (2016) 202–212, https://doi.org/10.1016/j.actamat.2016.02.050.

[32] J.M. Wheeler, J. Michler, Elevated temperature, nano-mechanical testing in situ in the scanning electron microscope, Rev. Sci. Instrum. 84 (4) (2013) 45103, https://doi.org/10.1063/1.4795829.

[33] C. Minnert, et al., New ultra-high temperature nanoindentation system for operating at up to 1100 °C, Mater. Des. 192 (2020) 108727, https://doi.org/10.1016/j.matdes.2020.108727.

[34] S. Bruns, et al., Room temperature viscous flow of amorphous silica induced by electron beam irradiation, Adv. Sci. 10 (7) (2023) e2205237.

[35] J.C. Trenkle, et al., Hot nanoindentation in inert environments, Rev. Sci. Instrum. 81 (7) (2010) 73901, https://doi.org/10.1063/1.3436633.

[36] C.A. Schuh, et al., Nanoindentation and contact-mode imaging at high temperatures, J. Mater. Res. 21 (3) (2006) 725–736, https://doi.org/10.1557/jmr.2006.0080.

[37] G. Tiphéne, et al., High-temperature scanning indentation: a new method to investigate in situ metallurgical evolution along temperature ramps, J. Mater. Res. 36 (12) (2021) 2383–2396, https://doi.org/10.1557/s43578-021-00107-7.

[38] G. Tiphéne, et al., Quantification of softening kinetics in cold-rolled pure aluminum and copper using high-temperature scanning indentation, Materials & Design 233 (2023) 112171, https://doi.org/10.1016/j.matdes.2023.112171.

[39] G. Tiphene, High-temperature scanning indentation (HTSI): compréhension des essais de nanoindentation lors des transformations physiques de matériaux métalliques à haute température, Ecole Centrale De Lyon (2023). https://theses.hal.science/tel-04117610/.

[40] E. Bruder, et al., Influence of solute effects on the saturation grain size and rate sensitivity in cu-X alloys, Scr. Mater. 144 (2018) 5–8, https://doi.org/10.1016/j.scriptamat.2017.09.031.

[41] W.C. Oliver, G.M. Pharr, An improved technique for determining hardness and elastic modulus using load and displacement sensing indentation experiments, J. Mater. Res. 7 (6) (1992) 1564–1583, https://doi.org/10.1557/JMR.1992.1564.

[42] W.C. Oliver, G.M. Pharr, Measurement of hardness and elastic modulus by instrumented indentation: advances in understanding and refinements to methodology, J. Mater. Res. 19 (1) (2004) 3–20, https://doi.org/10.1557/jmr.2004.19.1.3.

[43] D.L. Joslin, W.C. Oliver, A new method for analyzing data from continuous depth-sensing microindentation tests, J. Mater. Res. 5 (1) (1990) 123–126, https://doi.org/10.1557/JMR.1990.0123.

[44] J.M. Wheeler, J. Michler, Indenter materials for high temperature nanoindentation, Rev. Sci. Instrum. 84 (10) (2013) 101301, https://doi.org/10.1063/1.4824710.

[45] V. Maier, et al., Thermally activated deformation behavior of ufg-au: environmental issues during long-term and high-temperature nanoindentation testing, JOM 67 (12) (2015) 2934–2944, https://doi.org/10.1007/s11837-015-1638-7.

[46] R. Fleischer, Substitutional solution hardening, Acta Metall. 11 (3) (1963) 203–209, https://doi.org/10.1016/0001-6160(63)90213-X.

[47] N. Saunders, A.P. Miodownik, The cu-sn (copper-tin) system, Bull. Alloy Phase Diagr. 11 (3) (1990) 278–287, https://doi.org/10.1007/BF03029299.

[48] M. Conte, et al., Novel high temperature vacuum nanoindentation system with active surface referencing and non-contact heating for measurements up to 800 °C, Rev. Sci. Instrum. 90 (4) (2019) 45105, https://doi.org/10.1063/1.5029873.

[49] R. Limbach, et al., Strain-rate sensitivity of glasses, J. Non-Cryst. Solids 404 (2014) 124–134, https://doi.org/10.1016/j.jnoncrysol.2014.08.023.

[50] V. Maier, et al., Nanoindentation strain-rate jump tests for determining the local strain-rate sensitivity in nanocrystalline ni and ultrafine-grained al, J. Mater. Res. 26 (11) (2011) 1421–1430, https://doi.org/10.1557/jmr.2011.156.

[51] V. Maier-Kiener, K. Durst, Advanced nanoindentation testing for studying strain-rate sensitivity and activation volume, JOM 69 (11) (2017) 2246–2255, https://doi.org/10.1007/s11837-017-2536-y.